Automated large-scale and terrain-induced turbulence modulation of atmospheric surface layer flows in a large wind tunnel

Nasreldin O. Mokhtar ¹, Pedro L. Fernández-Cabán ², *, Ryan A. Catarelli ³

Keywords: multi-fan; turbulence; atmospheric surface layer; wind tunnel; integral length scales; large-scale testing

Abstract

1

2345

6 7

8

9

10

11 12

13 14

15

16

17 18

19

20

21

22

23

24

25

26

27

28

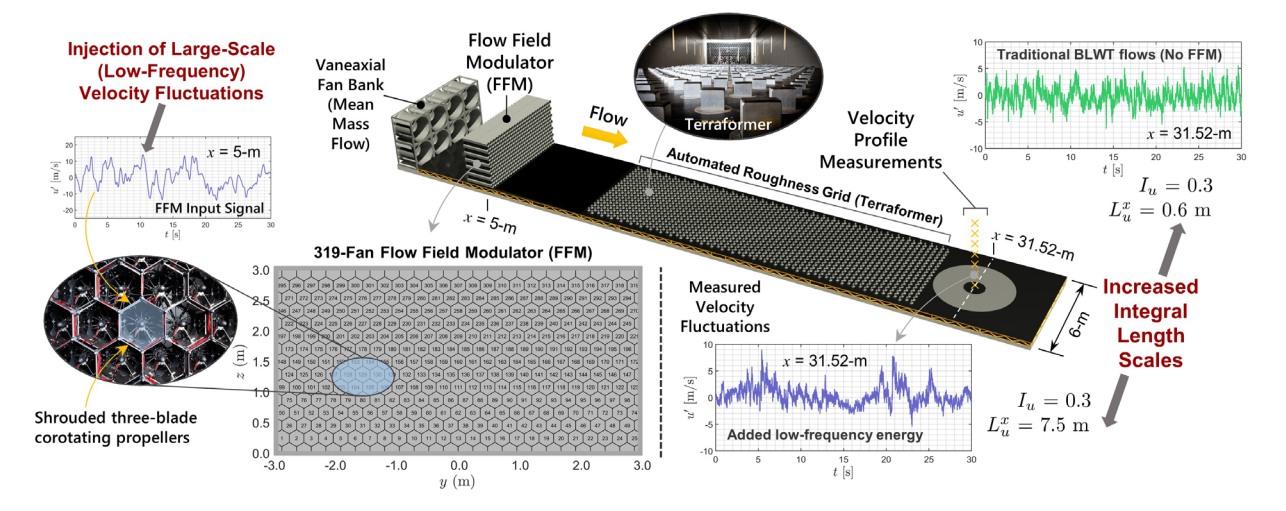
29

30

31 32

33 34 This study leverages a novel multi-fan flow-control instrument and a mechanized roughness element grid to simulate large- and small-scale turbulent features of atmospheric flows in a large boundary layer wind tunnel (BLWT). The flow-control instrument, termed the flow field modulator (FFM), is a computer-controlled 3 m × 6 m (2D) fan array located at the University of Florida (UF) Natural Hazard Engineering Research Infrastructure (NHERI) Experimental Facility. The system comprises 319 modular hexagonal aluminum cells, each equipped with shrouded three-blade corotating propellers. The FFM enables the active generation of large-scale turbulent structures by replicating userspecified velocity time signals to inject low-frequency fluctuations into BLWT flows. In the present work, the FFM operated in conjunction with a mechanized roughness element grid, called the Terraformer, located downstream of the FFM array. The Terraformer aided in the production of near-wall turbulent mixing through precise adjustment of the height of the roughness elements. A series of BLWT velocity profile measurement experiments were carried out at the UF BLWT test section for a set of turbulence intensity and integral length scale regimes. Input commands to the FFM and Terraformer were iteratively updated via a governing convergence algorithm (GCA) to achieve userspecified mean and turbulent flow statistics. Results demonstrate the capabilities of the FFM for significantly increasing the longitudinal integral length scales compared to conventional BLWT approaches (i.e., no active largescale turbulence generation). The study also highlights the efficacy of the GCA scheme for attaining prescribed target mean and turbulent flow conditions at the measurement location.

Graphical Abstract



¹ Florida A&M University–Florida State University, Tallahassee, FL, USA, <u>nasreldin1.mokhtar@famu.edu</u>

² Florida A&M University–Florida State University, Tallahassee, FL, USA, <u>plfernandez@eng.famu.fsu.edu</u>

³University of Florida, Gainesville, FL, USA, rcatarelli@ufl.edu

^{*}Correspondence

1 Introduction

Straight-line atmospheric surface layer (ASL) wind flows that interact with the built environment transport a broad range of turbulent scales (i.e., eddies). The size of turbulent fluctuations embedded in ASL flows can play a distinct yet equally critical role in the development of extreme wind pressures impinging on civil infrastructure. For decades, researchers and engineers have been successful in simulating the mean and turbulent velocity profile structure of ASL flows in boundary layer wind tunnels (BLWT) at relatively small simulation scales (e.g., < 1:100; Barlow et al. 1999; Simiu and Yeo 2019). At these reduced scales, the complete ASL turbulent wind spectrum can be physically simulated in long-fetch BLWTs via the inclusion of passive flow conditioning devices (spires, grids, roughness elements, castellated barriers, etc.) strategically located upstream of the testing section.

Recently, the commissioning of wind research facilities with increased cross-sectional dimensions (e.g., Standohar-Alfano et al. 2017; Chowdhury et al. 2017; Catarelli et al. 2020b) has enabled testing of larger models of civil structures (> 1:50) and brought with them several advantages over traditionally smaller wind tunnels: (1) higher wind velocities which can lessen the violation of Reynolds number similarity requirements, (2) enhanced spatial resolution of pressure sensors to accurately capture highly localized and extreme wind pressure fields, (3) and the addition of relatively small (minor) architectural building features (e.g., parapets, fins, etc.) that can mitigate wind effects. However, large-scale wind testing has also introduced challenges relating to the simulation of atmospheric flows. As wind tunnel simulation scales increase, the generation of larger turbulent gust structures by means of passive flow conditioning devices and long-fetch approaches (i.e., spire-roughness BLWT configurations) is often insufficient. Consequently, BLWT experiments conducted at geometric model scales of greater than 1:50 are often deficient in the production of large-scale (low frequency) turbulent fluctuations compared to analytical ABL models (Irwin 2008; Mooneghi et al. 2016).

Experimental studies (e.g., Melbourne 1979; Hillier and Cherry 1981; Gartshore 1984; Saathoff and Melbourne 1997) in BLWTs have demonstrated the significant role of both small- and large-scale freestream turbulence and their contribution to peak wind loads on sharp-edged bluff bodies (e.g., low-rise buildings). The presence of large-scale turbulence allows the vortices to attain maturity before being shed downstream away from the leading edge (Tieleman 2003). This results in higher peak suction pressures with increased duration. At the same time, small-scale turbulence is responsible for the flow structure near separation/reattachment zones (i.e., roof edges and corners). Consequently, the absence of either large- or small-scale turbulence in BLWTs often leads to the underestimation of extreme wind pressures (Tieleman 2003).

Physical simulation of small-scale turbulence in BLWTs can be readily achieved mechanically through the inclusion of roughness element (e.g., block) grids placed upstream of the testing section (e.g., Cook 1978; Shaw et al. 1982; Catarelli et al. 2020a). Roughness grids are passive in nature and their morphometric properties (e.g., 2D spacing and height) can be modified to modulate and increase near-surface turbulent mixing. On the other hand, precise control of large-scale gust structures through passive flow conditioning devices in BLWTs has proven challenging.

Active generation of large-scale turbulence in the BLWT has been attempted in previous works mainly through 2D active (or adjustable) grid systems placed upstream to the measurement location (e.g., Larssen and Devenport 2011; Knebel et al. 2011; Ramespacher et al. 2019; Neuhaus et al. 2021; Azzam and Lavoie 2023). Bienkiewicz et al. (1983) produced one of the early works which successfully introduce larger gust structures into a small BLWT (0.91 m square test section). In their study, actively generated turbulence was achieved via vertical in-plane grid oscillations of a pulsating grid consisting of equally spaced rectangular cylinders. The study found that turbulent scales generated using the pulsating grid approach were approximately one order of magnitude greater than scales produced by conventional (passive) turbulent grid arrays. A similar pulsating grid configuration was presented by Makita (1991), in which larger turbulence intensity and integral length scales were achieved in a small BLWT using a bi-plane active grid equipped with 15 vertical and horizontal oscillating rods. The study also commented on nonnegligible levels of anisotropy for the active turbulence cases considered. Both Bienkiewicz et al. (1983) and Makita (1991) focused on active control of the longitudinal (streamwise) velocity component.

Kobayashi and Hatanaka (1992) assessed the possibility of actively controlling the longitudinal and vertical flow velocity components through dynamic actuation of 2D arrays of plates and airfoils, respectively. The two arrays were arranged in series inside an Eiffel-type wind tunnel (0.7 m \times 1 m cross-section). The authors reported good agreement between target and measured longitudinal and vertical velocity fluctuations. However, excessively high turbulence generated by vortices induced by the plates and airfoils resulted in discrepancies for smoother flow conditions (i.e., low turbulence levels). Kobayashi et al. (1994) offered greater details regarding the active gust simulation procedure. These studies demonstrated the potential of control algorithms to achieve target power spectrum, integral scales of turbulence and turbulence intensity using sequential feedback control trials of active BLWT components.

Nishi et al. (1993) and Nishi and Miyagi (1995) disseminated some of the earliest studies aimed at simulating large-scale ABL turbulence in the BLWT using a computer-controlled multi-fan array system (as opposed to active grid systems). In these works, prescribed (target) mean velocity, turbulent intensity, and integral length scales were attained at the BLWT test section by iteratively adjusting the fan speeds of an 11×6 multi-fan array based on velocity sensor feedback. The study achieved maximum longitudinal integral length scale values of ~1.75 m at relatively low turbulence intensity levels (~6.5 %). Subsequent works were published to enhance the active simulation capabilities (e.g., inclusion of target Reynolds stresses) (Nishi et al. 1997; Nishi et al. 1999; Shuyang et al. 2001; Cao et al. 2002; Ozono et al. 2006). More recently, Ozono and Ikeda (2018) expanded their work to actively control high-intensity and large-scale turbulence. The study reported turbulence intensities between 12-16% and integral length scales 0.6-0.7 m.

The present study builds on previous research by leveraging a combined multi-stage flow conditioning system consisting of an active multi-fan flow-control instrument, termed flow field modulator (FFM), that works in conjunction with an automated (long-fetch) roughness element grid (called Terraformer) to precisely control and modulate both small- and large-scale turbulent features of ASL flows in a large BLWT. The primary goal of the study is to assess the effectiveness of the flow conditioning instruments (FFM and Terraformer) for increasing and tuning large-scale (particularly near-wall) ASL turbulent structures and enable future characterization of their impact on bluff body aerodynamics at relatively large BLWT scales (> 1:50).

The paper is divided into five sections. First, a description of the BLWT facility, flow conditioning components, instrumentation, and measurement techniques is provided in Section 2. The section also provides an explanation of the governing convergence algorithm (GCA) scheme used to achieve desired mean and turbulent flow properties at the BLWT test section. Section 3 highlights the results from a series of BLWT flow velocity measurements and provides a comparison to baseline (traditional) BLWT flows. Results found in Section 3 and their implications are then discussed in Section 4 and compared to findings obtained in other BLWT facilities. Finally, concluding remarks and future research directions are summarized in Section 5.

2 Experimental setup

 Flow measurement experiments were carried out at the University of Florida (UF) Natural Hazard Engineering Research Infrastructure (NHERI) Experimental Facility (EF) low-speed BLWT. The BLWT at UF is a (long-fetch) open circuit tunnel with dimensions of 6 m (W) \times 3 m (H) \times 38 m (L). The main UF BLWT flow conditioning components leveraged in the present work are highlighted in Fig. 1, and include a (1) vaneaxial fan bank, (2) the flow field modulator (FFM), and the (3) automated Terraformer roughness grid.

The vaneaxial fan bank consists of a 2×4 (vertical \times lateral) 448 kW fan array. The system is responsible for driving the mean mass flow along the BLWT, while active control of large-scale turbulent flow fluctuations is accomplished via the FFM, a high-resolution flow control device integrated into the upwind portion of the UF BLWT. The FFM is a computer-controlled 240 kW 2D array of 319 modular hexagonal aluminum cells containing shrouded three-blade corotating propeller pairs with high-performance 750-Watt brushless DC motors driven by electronic speed controllers (ESC). Command signals are sent to each of the 319 ESC by two NI cRIO-9048 eight slot chassis with NI-9403 C Series digital communication modules controlled by a custom FFM virtual instrument (VI). This hardware configuration permits a maximum free discharge velocity of +20/-17 m/s. The FFM 319 fan bank is located immediately upwind of the dimensionally identical 319 cell honeycomb system.

Smaller turbulent eddies are mechanically introduced into BLWT flows by means of the Terraformer roughness grid. The Terraformer is an 18 m (long-fetch) computer-controlled roughness array consisting of an array of 1116 (62 \times 18) integrated stepper motor assemblies that precisely rotate and translate roughness elements independently from one another to control height and aspect ratio. Each roughness element has a rectangular plan dimension of 5 cm \times 10 cm and the heights can vary from 0 cm (element flush with tunnel floor) to 16 cm. Additional information regarding the BLWT can be found in Catarelli et al. (2020a; 2020b).

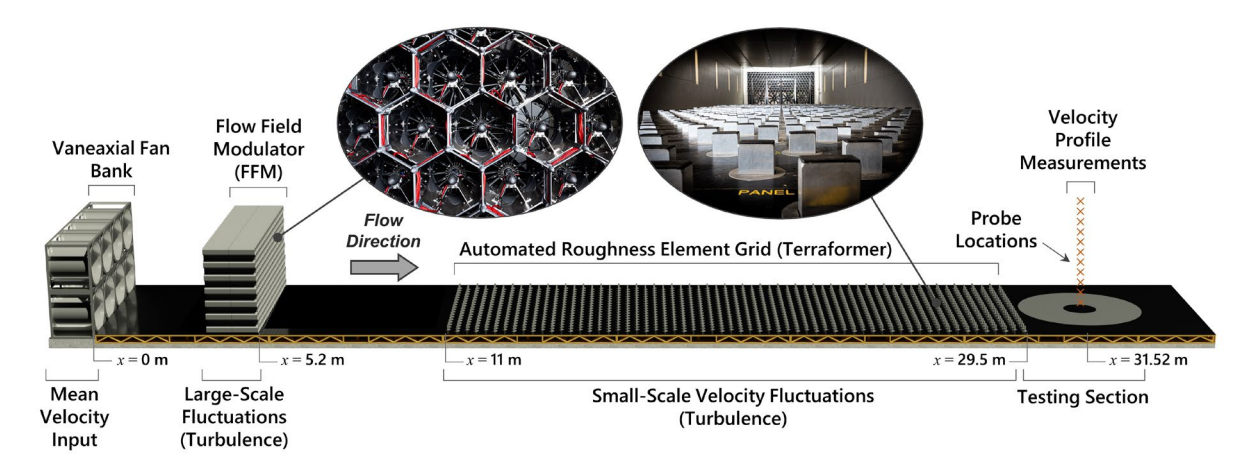


Fig. 1 UF BLWT flow conditioning components

Three-dimensional (u, v, and w) velocity flow data were collected at the center of the downwind BLWT test section (BLWT location x=31.52 m, y=0 m). The BLWT flow measurement setup is presented in Fig. 2. Velocity profile measurements were taken using 12 five-hole Vectoflow velocity probes mounted to an automated instrument traverse system. A redundant Cobra probe velocity sensor from Turbulent Flow Instrumentation (TFI) was located at a reference height $z=z_{ref}=19.8$ cm. Vectoflow probes were set to measurement heights z=5,10,15,19.8,25,30,52.5,72.5,95,115,137.5, and 157.5 cm above the tunnel floor. The measurement heights were selected to ensure that at least one velocity sensor is within the height of each of the bottom eight FFM cell rows, while the reference height $z_{ref}=19.8$ cm corresponds to the roof eave height of a 1:20 reduced scale version of the Wind Engineering Research Field Laboratory (WERFL) test building (Levitan and Mehta 1992a, 1992b). The latter was chosen to examine the influence of FMM-generated integral length scales on aerodynamic effects in subsequent BLWT pressure loading experiments. Both Vectoflow and Cobra probe time history data were sampled at 850 Hz and low-pass filtered during post-processing using a 3^{rd} order Butterworth filter and a cutoff frequency of 150 Hz.

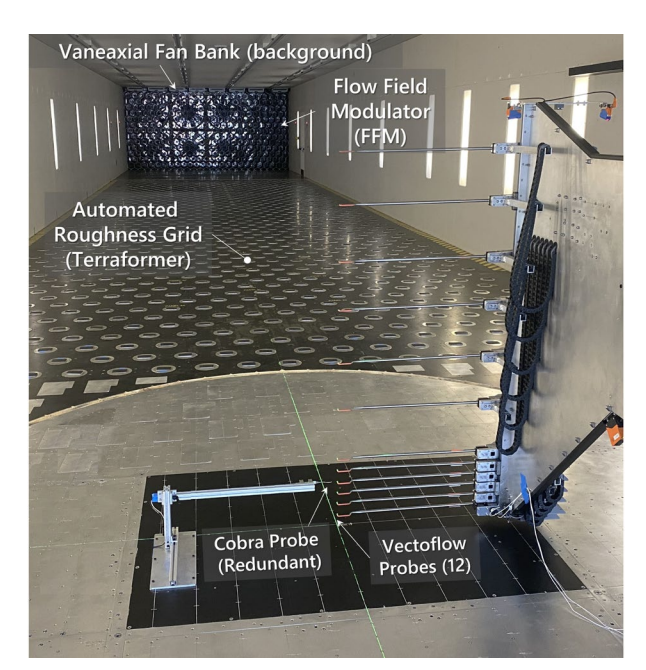


Fig. 2 Experimental BLWT setup for velocity profile measurements

2.1 Mean and turbulent velocity fluctuations

Instantaneous flow velocity time histories $u_i(t)$ taken at an arbitrary point in space were decomposed into mean (\bar{u}_i) and fluctuating (turbulent) $u_i'(t)$ parts (i.e., Reynolds decomposition) as follows:

$$u_i(t) = \bar{u}_i + u_i'(t) \tag{1}$$

where the subscript i indicates the longitudinal (streamwise; i = 1), lateral (spanwise; i = 2), and vertical velocity (i = 3) components. In this study, the three velocity components will be represented by $u = u_{i=1}$, $v = u_{i=2}$, and $w = u_{i=3}$. Axis rotation was performed on the Vectoflow and Cobra probe velocity data to align the longitudinal velocity component (u) in the direction of the mean wind flow (Foken and Nappo, 2008) and neglect the mean velocity of the lateral (v) and vertical (v) components (i.e., $\bar{v} = 0$ and $\bar{w} = 0$).

In wind engineering, Reynolds stresses are often represented in terms of turbulence intensity:

$$I_i = \frac{\sigma_i}{\bar{u}} \tag{2}$$

in which I_i is the turbulence intensity for the longitudinal (i = 1), lateral (spanwise; i = 2), and vertical velocity (i = 3) components of the flow, σ_i is the standard deviation, and \bar{u} is the longitudinal mean wind velocity.

 Large-scale turbulent fluctuations of ABL flows are commonly characterized by integral length scales. Taylor's "frozen" turbulence approximation was assumed to estimate integral length scales along the longitudinal (x) dimension for the three velocity components by integration of the autocorrelation function:

$$L_i^x = \bar{u} \int_0^\infty \rho_{ii}(\tau) d\tau \tag{3}$$

where τ is the time lag and the autocorrelation function is defined as:

$$\rho_{ij}(\tau) = \frac{\overline{u_i'(t)u_j'(t+\tau)}}{\overline{u_i'(t)u_i'(t)}} \tag{4}$$

2.2 Governing Convergence Algorithm (GCA)

three-stage flow conditioning system—i.e., vaneaxial fans (Stage 1), FFM (Stage 2), and Terraformer (Stage 3). The controls of the combined system were driven by a governing convergence algorithm (GCA), which accepts user-specified target mean, turbulence intensity, and integral length scale profiles as inputs. System control inputs (e.g., FFM fan RPM, Terraformer height, etc.) were generated by the GCA and loaded to each stage by the BLWT operator. The GCA then makes iterative adjustments to the three control stages using a proportional integral derivative (PID)

The mean and turbulent properties at the center of the BLWT testing section were controlled thorough an automated

based closed-loop control scheme consisting of multiple independent control loops.

Target mean velocity and turbulent flow properties for 12 representative GCA events are listed in Table 1. Target GCA longitudinal (streamwise) mean velocity, turbulence intensity, and integral length scale profiles were based on empirical power law models of ABL flows provided in ASCE 7-22 (2021). The target mean velocity model was determined according to:

$$\bar{u}(z) = \bar{u}_{ref} \left(\frac{z}{z_{ref}}\right)^{\alpha} \tag{5}$$

were $\bar{u}(z)$ is the target mean longitudinal velocity at elevation z, \bar{u}_{ref} is the mean velocity at a reference elevation z_{ref} , and α is the terrain constant. The target longitudinal turbulence intensity was computed as follows:

$$I_u(z) = I_{u,ref} \left(\frac{z_{ref}}{z}\right)^{\beta} \tag{6}$$

192 193

in which $I_u(z)$ is the turbulence intensity (i.e., $\sigma_u(z)/\bar{u}(z)$) at elevation z, and β is the terrain constant for turbulence intensity (= 1/6). Finally, target integral length scales were computed from:

194 195

$$L_u^{\chi}(z) = L_{u,ref}^{\chi} \left(\frac{z}{z_{ref}}\right)^{\gamma} \tag{7}$$

196 197

In Eq. 7, $L_u^x(z)$ is the length scale at elevation z and γ is the terrain constant for integral length scales.

198 199

The modulation of large-scale turbulence (i.e., L_u^x) is achieved by the FFM. The von Kármán model (1948) of isotropic turbulence was used as the target turbulent spectra for the GCA:

200 201

$$S_{uu}(z,f) = \frac{4L_u^x I_u^2 \,\bar{u}}{f[1 + 70.8(fL_u^x/\bar{u})^2]^{5/6}}$$
(8)

202 203

where $S_{uu}(z, f)$ is the power spectral density function of the longitudinal velocity component and f is the frequency. Given the relatively long distance between the FFM and the measurement location (Fig. 1), modifications (i.e., spectral warping) to the FFM velocity (input) time signals were autonomously performed by GCA to achieve the desired spectral characteristics at the downwind test section.

205 206 207

204

The error signal for the mean profile segment for each FFM cell row follows the form:

$$e_{\bar{u}}^i(z) = \bar{u}_T(z) - \bar{u}_M^i(z) \tag{9}$$

208 209

where $\bar{u}_T(z)$ is the target mean profile and $\bar{u}_M^i(z)$ is the measured profile of the *i*-th iteration as a function of elevation z. The computed $e_{\overline{u}}^{i}$ is then used to adjust the input mean velocity of the next GCA iteration:

$$\bar{u}^{i+1}(z) = \bar{u}^i(z) + e^i_{\bar{u}}(z) \times K_p \tag{10}$$

210

where $\bar{u}^i(z)$ is the input mean velocity in the *i*-th iteration and K_p is the proportional gain.

211 212

The spectral warping technique used in the study follows a modification of the Cao et al. (2002) process involving the calculation of an error signal for each frequency in the measured power spectrum at each z position:

$$e_{S_{nn}}^{i}(z,f) = S_{T}(z,f) - S_{M}^{i}(z,f)$$
(11)

213

where $S_T(z,f)$ are the target power spectra and $S_M^i(z,f)$ are the measured power spectra of the *i*-th convergence iteration. The computed e_{Suu}^i is then used to warp the input power spectra of the next GCA iteration: 214

$$S_{uu}^{i+1}(z,f) = S_{uu}^{i}(z,f) + e_{S_{uu}}(z,f) \times K_{pw}$$
 (12)

- 215
- where $S_{uu}^i(z,f)$ is the current power spectral input and K_{pw} is warping gain used to adjust the convergence rate and
- 216 limit system instabilities. PID controller tuning was performed to efficiently damp the system (i.e., limit overshoot of
- 217 and oscillation around the target profiles) heuristically following the classical Ziegler-Nichols method. The gains used
- 218 for final convergence were $K_p = 3$, $K_i = 1$, and $K_d = 0$. The warping gain for the synthetic turbulence modulation
- 219 function was $K_{pw} = 30$. Additional information regarding the specific spectral warping and PID control algorithm and
- 220 tuning parameters can be found in Pinyochotiwong (2022).

Table 1 GCA target mean and turbulent flow statistics ($z_{ref} = 19.8 \text{ cm}$)

Event		ean ocity		ılence nsity	Integral Length Scale		
Lvent	\bar{u}_{ref} (m/s)	1/α	$I_{u,ref}$	1/β	$L_{u,ref}^{x}$ (m)	1/γ	
EVT01	6.0	11	0.15	6	1.0	8	
EVT02	6.0	9	0.20	6	1.0	5	
EVT03	6.0	7	0.30	6	1.0	3	
EVT04	6.0	11	0.15	6	3.0	8	
EVT05	6.0	9	0.20	6	3.0	5	
EVT06	6.0	7	0.30	6	3.0	3	
EVT07	6.0	11	0.15	6	5.0	8	
EVT08	6.0	9	0.20	6	5.0	5	
EVT09	6.0	7	0.30	6	5.0	3	
EVT10	6.0	11	0.15	6	7.0	8	
EVT11	6.0	9	0.20	6	7.0	5	
EVT12	6.0	7	0.30	6	7.0	3	

A flowchart of the GCA iteration sequence is illustrated in Fig. 3. First, the three-stage flow conditioning system is configured using initial GCA inputs to the vaneaxial fans, FFM, and Terraformer and a maximum number of iterations is set. Second, the Terraformer is actuated to adjust the roughness height. Third, the vaneaxial fans are brought up to (constant) speed. Fourth, the FFM fan array is triggered, and each electronic speed controller is given a prescribed velocity time signal. Fifth, flow measurements are collected at the downwind BLWT test section. Sixth, velocity profile data are processed and errors between the target (i.e., von Kármán) and measured longitudinal velocity spectra at each z measurement height are computed. System inputs are updated to reduce the error signals using the tuned PID gains. Finally, these steps are repeated until user-specified convergence criteria are met.

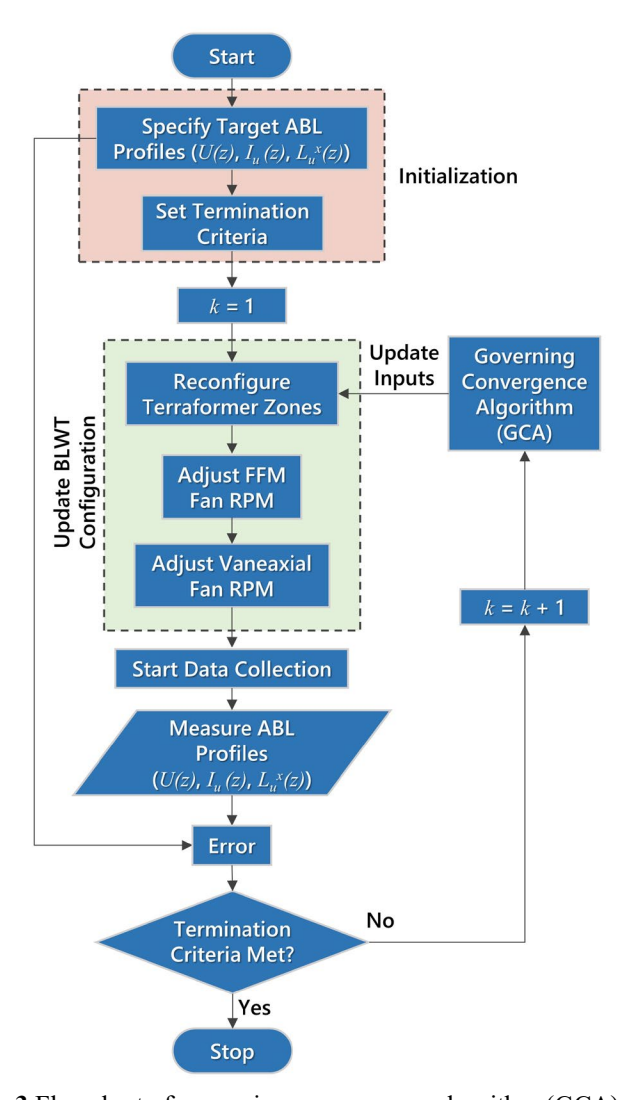


Fig. 3 Flowchart of governing convergence algorithm (GCA)

GCA input controls are illustrated in Fig. 4. Vaneaxial fan (VF) inputs consist of two control variables where (constant) fan speeds are set for the top and bottom rows (VF1 and VF2). Eight GCA inputs (i.e., FFM 1, FFM 2, ..., FFM 8) correspond to the FFM cell rows closest to the BLWT floor. FFM input files consist of velocity time series that are responsible for the production (i.e., injection) of large-scale turbulence. Lastly, for GCA purposes, the Terraformer roughness grid is discretized into six zones (TF1, TF2, ..., TF6) of uniform roughness heights.

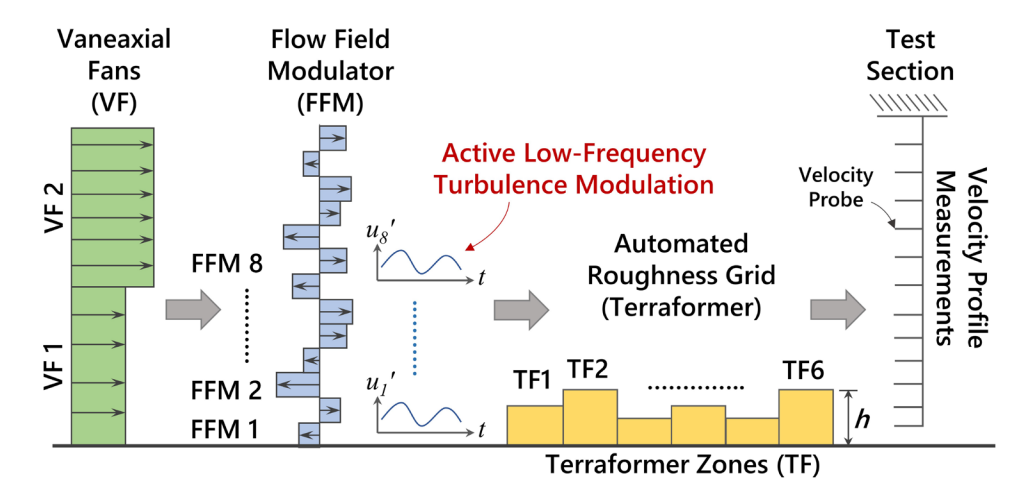


Fig. 4 BLWT input controls for GCA

The specific GCA termination criteria are typically a user-specified scalar metric of (1) root mean square (RMS) error for each target profile or (2) maximum number of iterations (k_{max}). The latter was implemented in this work and the maximum number of iterations was set to $k_{max} = 25$. However, to increase experimental efficiency, velocity profile data for early GCA iterations (k = 1-10) were collected for 30 s, k = 11-24 were sampled for 60 s, and the final iteration was performed for 200 s.

The GCA convergence process is designed to minimize the RMS error (a scalar distance metric) between the target and mean profile independently for each of the FFM cell rows (shown in Fig. 4), while simultaneously minimizing the RMS errors of the target and measured power spectra of each cell row. The warping of the input spectra (S_{uu}^i) and subsequent matching of the output spectra at each height results in convergence of the I_u and L_u^x profiles. Independently converging the mean profile ensures that the spectral matching will not result in an ill-fitting condition. A summary of the GCA settings for each flow conditioning and sensing BLWT components is provided in Table 2.

Table 2 UF BLWT components and GCA settings

	Table 2 of BE W T components and correctings								
BLWT Component	Primary Function	Instrument Range	Instrument Array	Control Settings	Longitudinal (streamwise) Location in BLWT (m)				
Vaneaxial Fans	Mean mass flow input	0-17 m/s (constant velocity)	8 (2 × 4)	2 (top and bottom rows)	x = 0 m				
Flow Field Modulator (FFM)	Large-scale turbulent fluctuations	+20/-17 m/s (velocity)	319 (13)	8 (vertical cell rows)	x = 5.2 m				
Terraformer	Small-scale (terrain- induced) turbulent fluctuations	0–16 cm (roughness element height)	1162 (62 × 18)	6 (roughness zones)	x = 11-14.2 m (Zone 1), 14.2-17.4 m (Zone 2), 17.4-20.6 m (Zone 3), 20.6-23.8 m (Zone 4), 23.8-27 m (Zone 5), 27-29.5 m (Zone 6)				
Vectoflow Probe rake	3D flow measurements	-	12 × 1	-	x = 31.52 m				

3 Results and Analysis

3.1 Target and measured mean and turbulent flow statistics

Representative longitudinal (streamwise) mean velocity, turbulence intensity, integral length scale profiles measured at the center of the downwind BLWT test section (x = 32.52 m) are illustrated in Fig. 5 for EVT12 (see Table 1),

which corresponds to the GCA event targeting highest I_u (30%) and L_u^x (7 m) specified at the reference height (z_{ref} = 19.8 cm). Measurement points proximate to (i.e., immediately above and below) z_{ref} = 19.8 m demonstrate very good agreement between the target profile statistics (solid red line) and the best GCA iteration (cyan markers). In this work, the term "best" iteration is adopted to represent the k value that most closely matches the target L_u^x at z = 19.8 cm specified for each event (Table 1)—i.e., the "best" iteration may not correspond to the "final" iteration (k_{max}). GCA runs (gray 'o' markers) depicted in Fig. 5 also reveals the broad range of possible L_u^x scales at the BLWT test section through the full vertical extent of the profile. For instance, length scales of approximately 2 m and 14 m were independently detected by the Vectoflow and (redundant) Cobra probe at the reference height. Yet, some of the higher length scales were estimated from early runs with relatively short durations (e.g., 30 s) and longer sampling times may be necessary to reliably estimate L_u^x . Table 3 reports the mean velocities and turbulent scales—length (L_u^x) and time (T_u)—at the reference height for all 12 events.

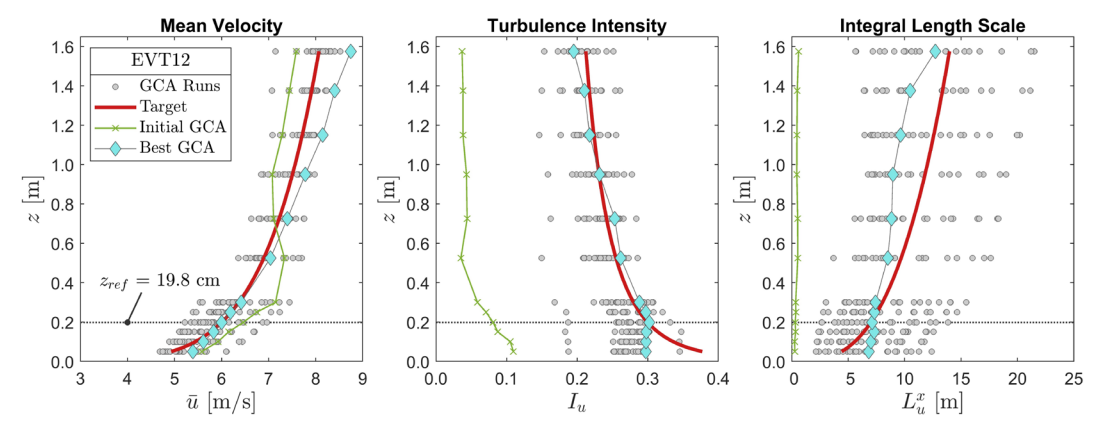


Fig. 5 GCA generated mean velocity, turbulent intensity, and integral length scale profiles for EVT12

A representative GCA iteration history of the mean percent error (measured vs. target) derived from the 12 Vectoflow profile elevations is depicted in Fig. 6 for EVT12. Relatively low mean errors of $\bar{u}(z)$ are displayed through the entire iteration process, which indicates that the vaneaxial fans can rapidly tune the mean mass flow to achieve the target mean profile (Eq. 5). Fig. 6 also shows $I_u(z)$ profiles to stabilizing after ~8 GCA iterations, followed by a slight increase in the mean error during late stages of the iteration process. The most considerable fluctuation in mean error was observed in $L_u^x(z)$, which displayed errors ~25% for k > 12. The "jagged" nature of the mean error in $L_u^x(z)$ profiles is expected, given the relatively high uncertainty levels of this turbulent parameter (compared to $\bar{u}(z)$ and $I_u(z)$). A more detailed statistical analysis to quantify the uncertainty of integral time and length scale estimates is presented in Section 3.5.

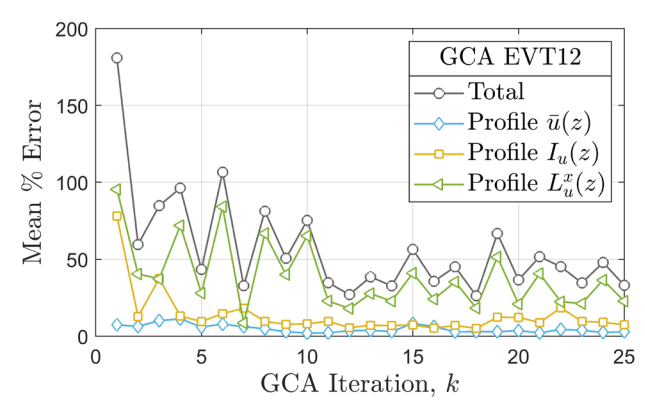


Fig. 6 GCA iteration history of percent error between measured and target mean and turbulent profile flows (EVT12).

Table 3 Mean velocity and integral length and time scales measured at $z_{ref} = 19.8$ cm (x = 31.52 m)

Event	Target $I_{u,T}$	Best GCA Iteration, k	<i>ū</i> [m/s]	ū Error [%]	<i>T_u</i> [s]	$L_u^x = \bar{u}T_u$ [m]	$L_{u,T}^{x}$ [m]	L_u^x Error [%]	$L_u^x/L_{u,Baseline}^x$
Baseline ¹ 1	0.15	_	8.84	-	0.12	1.07	-	-	-
EVT01		5	5.90	1.7	0.19	1.15	1.0	15.0	1.1
EVT04		4	6.03	0.5	0.70	4.22	3.0	40.7	3.9
EVT07		3	5.94	1.0	0.85	5.06	5.0	1.2	4.7
EVT10		8	5.94	1.0	1.07	6.35	7.0	9.3	5.9
Baseline 2	0.20	•	7.63	•	0.11	0.87	ı	•	-
EVT02		8	5.70	5.0	0.30	1.73	1.0	73.0	2.0
EVT05		22	5.82	3.0	0.49	2.87	3.0	4.3	3.3
EVT08		4	6.15	2.5	0.92	5.68	5.0	13.6	6.5
EVT11		3	6.34	5.7	1.26	7.99	7.0	14.1	9.1
Baseline 3	0.30	-	6.23	-	0.09	0.58	-	-	-
EVT03		24	4.94	17.7	0.20	0.99	1.0	1.0	1.7
EVT06		22	5.14	14.3	0.51	2.61	3.0	13.0	4.5
EVT09		8	5.49	8.5	0.89	4.91	5.0	1.8	8.5
EVT12		12	6.05	0.8	1.22	7.40	7.0	5.7	12.8
¹ Baseline = no active FFM turbulence modulation									

The convergence history of the GCA at the reference height ($z_{ref} = 19.8$ cm) for the three events with target length scales $L_{u,T}^x = 7$ m are depicted in Fig. 7. For lower turbulence levels (e.g., $I_{u,T} = 0.15$ and 0.20), GCA consistently undershoots the target length scale as it steadily approaches the desired value. For instance, EVT10 and EVT11 demonstrate a congregation of GCA iterations in the range $L_u^x = 4$ m and 7 m. Conversely, EVT12 ($I_{u,T} = 0.30$) shows a greater dispersion of GCA iterations and some exceeding the target length scale > 7 m. The larger spread may be attributed to the influence of significantly augmented roughness elements to achieve the relatively high target I_u (see Section 3.4).

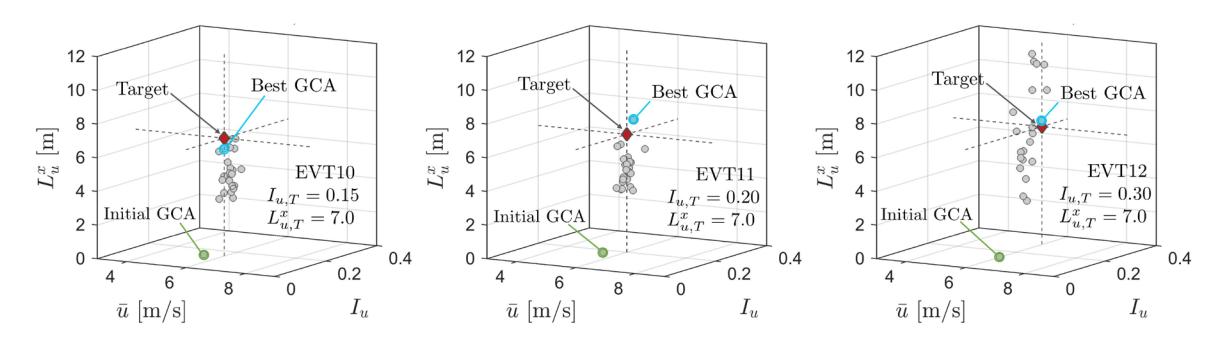


Fig. 7 Distribution of measured mean and turbulent flow statistics ($z_{ref} = 19.8$ cm)

3.2 Injection of low-frequency turbulence

FFM input velocity traces for the best GCA runs displayed significantly larger fluctuations to achieve the desired (target) L_u^x at the measurement location (x = 32.52 m). For example, Fig. 8 shows the input velocity time trace delivered to the electronic speed controllers of the lowest FFM cell row and the corresponding longitudinal flow velocity time history captured at the downwind test section. The two signals correspond to the best GCA run for EVT12 (target $I_{u,T} = 0.3$ and $L_{u,T}^x = 7$ m). It is worth noting that the FFM input signal (blue) and measured (green) velocity traces in Fig. 8 are not time-synced, and therefore reliable quantification of the advection time of low frequency gusts traveling from the FFM to the measurement location (x = 32.52 m) was not possible. Nevertheless, the purpose of Fig. 8 is to highlight the relative amplitude (input vs. output) of low-frequency fluctuations needed to achieve the desired $L_{u,T}^x$. The power spectral density subplot in Fig. 8 also reveals the injection of low-frequency (< 3 Hz) energy by the FFM (blue spectra curve) to obtain the target $L_{u,T}^x$.

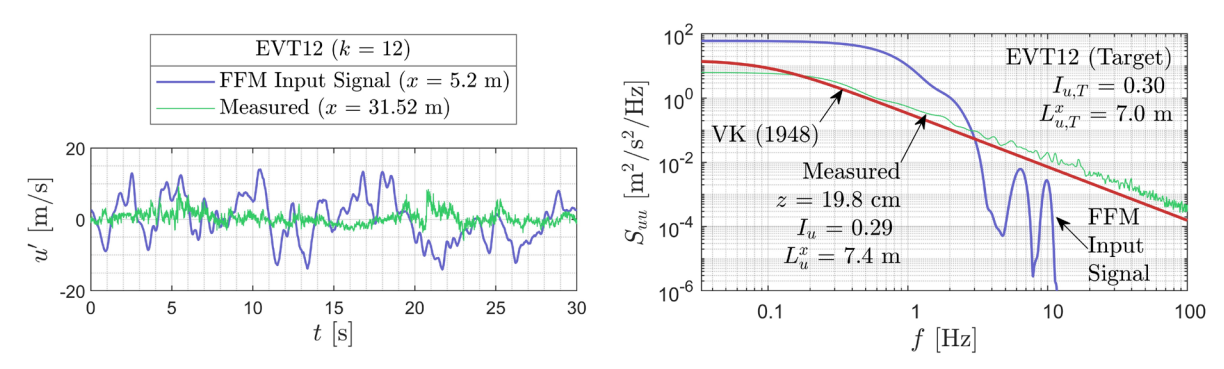


Fig. 8 Time history and power spectra of measured and FFM input longitudinal flow velocity fluctuations

3.3 Spectral analysis and temporal correlation of velocity fluctuations

Nondimensional longitudinal (streamwise) power spectra plot for all 12 events measured at the downwind test section $(z_{ref} = 19.8 \text{ cm})$ are included in Fig. 9. Each spectrum was computed using Welch's method (Bendat and Piersol, 2000). Time histories were segmented into 10 contiguous blocks, and a Hanning tapering window with 50% overlap was applied to suppress side-lobe leakage. The baseline case (gray curves) represents traditional BLWT tests with no (active) FFM flow fluctuations. The three subplots display a systematic leftward shift (i.e., towards lower frequencies) with increasing L_u^x . The shift is more evident for larger turbulence levels ($I_{u,T} = 0.3$). Further, for the same turbulence intensity, spectra curves with lower L_u^x show higher energy in the inertial subrange to account for the missing low-frequency energy.

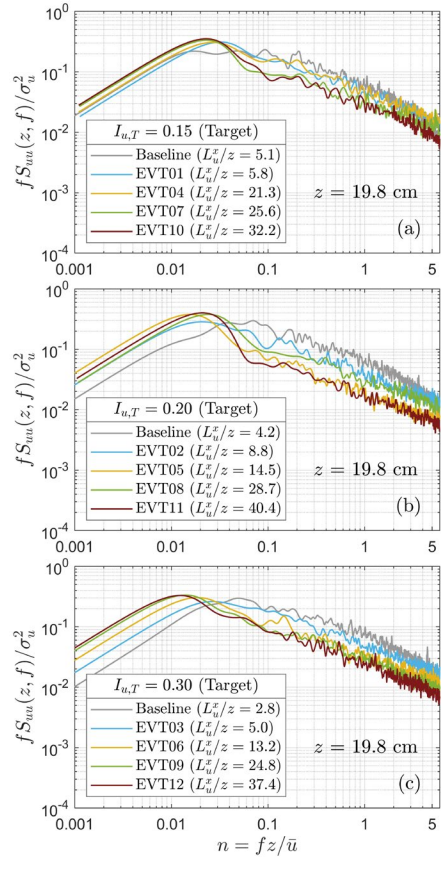


Fig. 9 Nondimensional longitudinal (streamwise) power spectra for all 12 GCA events ($x = 31.52 \text{ m}, z_{ref} = 19.8 \text{ cm}$)

312313

314

315316

317318

As previously noted, integral length scales were estimated via integration of the autocorrelation function $(\rho(\tau))$ of the fluctuating wind velocity component (and the adoption of Taylor's hypothesis). Illustrative $\rho_{uu}(\tau)$ subplots for four GCA events with target turbulence intensities of $I_{u,T}=0.15$ are presented in Fig. 10. The sublots display the delay in the (first) zero-crossing point (i.e., $\rho_{uu}(\tau)=0$) as L_u^x is increased. For instance, EVT01 reaches $\rho_{uu}(\tau)=0$ at around 1.2 s, while the zero-crossing point for EVT10 occurs at approximately 5.5 s. EVT04 and EVT07 show very similar time lags (~3.7 s). The autocorrelation functions for the vertical component $\rho_{ww}(\tau)$ for the same four GCA events depicted in Fig. 10 are included in Fig. 11. Results from the $\rho_{ww}(\tau)$ subplots suggest that the noticeable delay to reach $\rho_{uu}(\tau)$ is not observed in the vertical component where L_w^x values were only doubled when comparing EVT01 and EVT03. Similar trends were detected for the other eight events with higher turbulent levels.

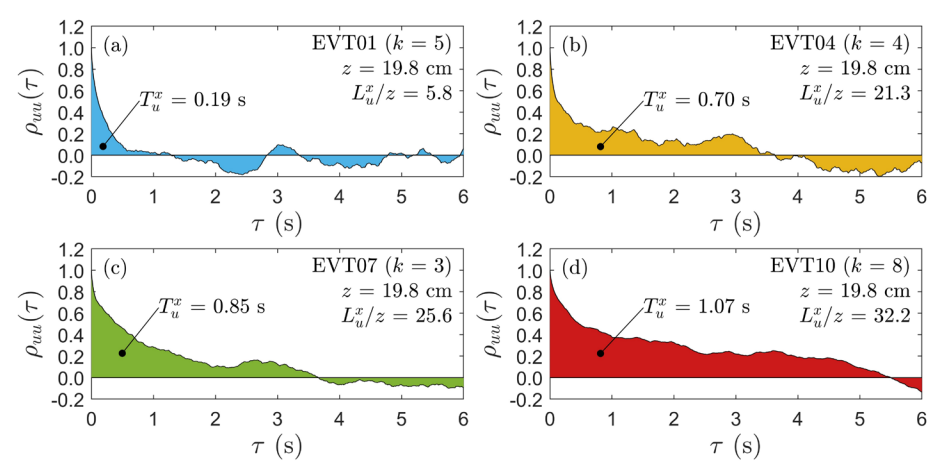


Fig. 10 Autocorrelation functions of longitudinal (streamwise) velocity fluctuations of best GCA run for (a) EVT01, (b) EVT04, (c) EVT07, and (d) EVT10 (x = 31.52 m, $z_{ref} = 19.8$ cm)

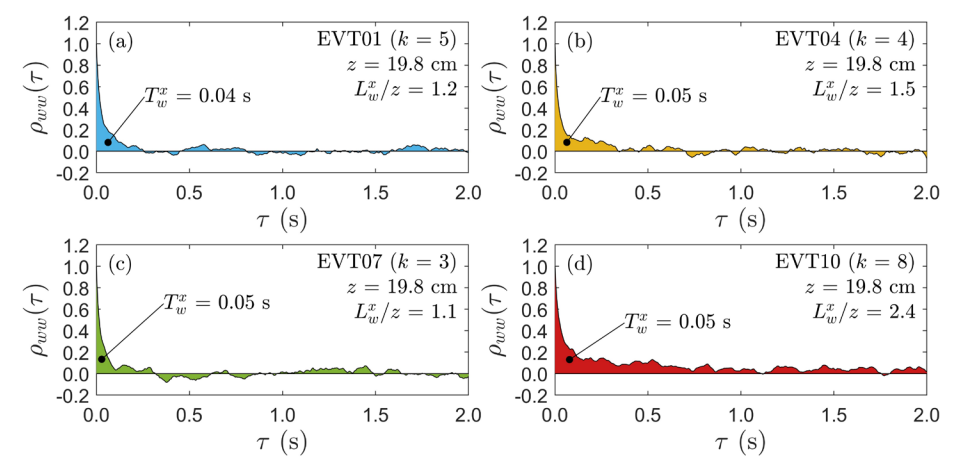


Fig. 11 Autocorrelation functions of vertical velocity fluctuations of best GCA run for (a) EVT01, (b) EVT04, (c) EVT07, and (d) EVT10 ($x = 31.52 \text{ m}, z_{ref} = 19.8 \text{ cm}$)

3.4 Mechanical (terrain-induced) turbulence

Systematic analysis of the results obtained by the GCA revealed the predominant effect of the Terraformer roughness grid for controlling near-surface turbulence intensity (I_u) at the downwind test section. Specifically, the levels of mechanically generated turbulence needed to achieve the roughest GCA events $(I_u = 0.3)$ were autonomously enabled through optimal adjustment of the roughness element heights (h) at each Terraformer zone. Further, the Terraformer

zone closest to the test section (i.e., TF6) appeared to offer the greatest influence on near ground I_u values. This behavior can be inferred from a comparison of roughness element heights (h) reported in Table 4. When considering all 12 events, the highest roughness heights were leveraged by EVT03 and EVT06 to attain $I_u = 0.3$ (h = 160 mm and h = 142 mm, respectively, in the case of TF6). However, EVT09 and EVT12 also targeted 30% turbulence levels but GCA was able to approach $I_{u,T}$ with noticeably lower roughness element heights (h = 87 mm and h = 65 mm, respectively; TF6). The diminishing reliance on mechanically generated turbulence by the roughness grid with increasing L_u^x indicates greater contribution of large-scale turbulence to I_u .

Table 4 Terraformer zonal roughness configuration for best GCA iteration.

Event	Best GCA Iteration, k	Roughness Element Height, h [mm]						I_u (z = 19.8 cm)		% Error
		TF1	TF2	TF3	TF4	TF5	TF6	BLWT	Target	(Absolute)
EVT01	5	10	12	12	37	24	17	0.14	0.15	8.6
EVT02	8	17	18	16	52	30	45	0.19	0.20	7.3
EVT03	24	27	36	15	144	60	160	0.27	0.30	8.8
EVT04	4	10	10	10	23	18	16	0.13	0.15	12.6
EVT05	22	23	10	10	31	10	26	0.24	0.20	18.6
EVT06	22	29	27	22	82	10	142	0.33	0.30	9.9
EVT07	3	10	10	10	24	18	13	0.15	0.15	0.5
EVT08	4	10	10	10	25	17	22	0.16	0.20	19.7
EVT09	8	22	23	26	65	52	87	0.29	0.30	3.7
EVT10	8	31	14	17	25	10	10	0.16	0.15	4.0
EVT11	3	25	10	10	13	10	12	0.19	0.20	6.7
EVT12	12	28	18	23	38	30	65	0.29	0.30	2.3

An illustrative visual of the iterative (GCA-driven) adjustments to zonal roughness element heights is presented in Fig. 12 for the three events with the largest target length scales ($L_{u,T}^x = 7$ m). Roughness element heights (vertical axes) were normalized by the reference probe measurement height (h/z_{ref} ; where $z_{ref} = 19.8$ cm). The circular (blue) markers represent the h/z_{ref} for each of the sequential 25 GCA iterations, while the six gray cuboids indicate the zonal roughness heights for the best GCA iteration. Subplots corresponding to target turbulence levels of 15% and 20% (Fig. 12a and 12b) display comparable roughness configurations for the six Terraformer zones. In both GCA events, the highest roughness heights occurred at the start of the Terraformer grid (i.e., TF1). Small variability in h/z_{ref} is observed for the remaining five roughness heights downstream of TF1. In contrast, Fig. 12c (EVT12) shows significant variability in h/z_{ref} along the six discrete TF zones and taller roughness elements toward the end of the Terraformer. A similar (albeit more pronounced) morphology in TF zonal heights was observed for GCA events with $I_{u,T} = 0.3$ and $I_{u,T}^x < 7.0$ m (Table 4).

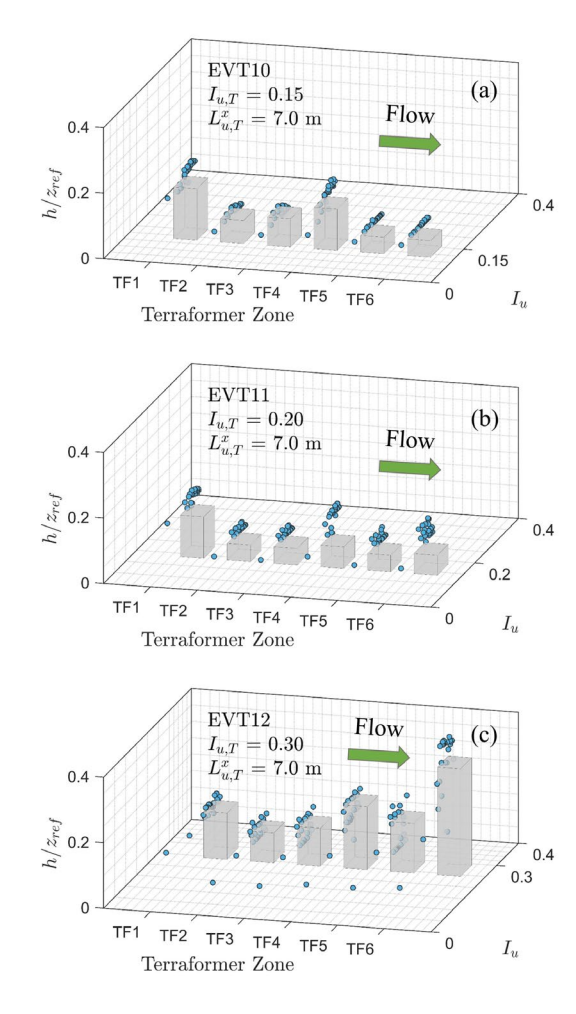


Fig. 12 Roughness heights of Terraformer (TF) zones for GCA events (a) EVT10, (b) EVT11, and (c) EVT12 ($z_{ref} = 19.8 \text{ cm}$)

3.5 Uncertainty estimates of integral length scales

Execution of the GCA in the BLWT requires sequential iterations which can increase experimental time. As previously stated, the present study applied short-interval sampling durations for early GCA iterations that were incrementally increased until the termination criteria were reached. However, the accuracy of L_u^x estimates can be strongly influenced by the sampling time, which must be sufficiently long to ensure that an acceptable number of large-scale turbulence structures (i.e., eddy cycles) are experimentally captured.

To investigate and quantify the statistical error in L_u^x estimates, a supplemental 8-min (480 s) flow measurement experiment was carried out using the inputs of the vaneaxial fans, FFM, and Terraformer associated with the best GCA iteration of EVT07 (which produced $L_u^x = 5.06$ m for the original 30 s record; see Table 3). A moving block bootstrap technique (MBB) presented in Garcia et al. (2006) was applied to the 8-min record. This MBB procedure has been specifically validated to provide good approximations of confidence intervals of integral time and length scales of turbulent flows. The MBB technique first computes an optimal block length (b_{opt}) of the velocity signal. The present study adopted the approach detailed in Politis and White (2004) to calculate b_{opt} through minimization of the mean square error (MSE) of the variance of the sample mean parameter:

$$b_{opt} = \left(\frac{2G^2}{D}\right)^{1/3} N^{1/3} \tag{13}$$

$$g(0) = \sum_{k=-M}^{M} \lambda(k/M) \times \rho_{uu}(\tau)$$
(14)

$$G = \sum_{k=-M}^{M} \lambda(k/M) \times |k| \times \rho_{uu}(\tau)$$
(15)

In Eq. 13, 14, and 15, $D = 4/3g(0)^2$, N is the total length of the velocity signal, k is the lag vector, M = 2m where m is the smallest integer after which the autocorrelation function is negligeable (i.e., $\rho_{uu}(\tau) \approx 0$). In Eq. 14 and 15, $\lambda(k/M) = 1$ if $0 \le |k/M| \le 0.5$, $\lambda(k/M) = 2(1-|k/M|)$ if $0.5 \le |k/M| \le 1$, and $\lambda(k/M) = 0$ otherwise.

After applying Eq. 13 to the autocorrelation function and time lags of the 8-min velocity signal, a moving block length of $b_{opt} = 5074$ ($b_{opt}\Delta t = 5.97$ s, where $\Delta t = 1/850$ Hz) was obtained. In their work, Garcia et al. (2006) also provided an empirical relation of the moving block length in terms of the integral time scale (T_u) and sampling time (T_d) of the full velocity signal as $b_{opt}\Delta t = 0.788T_u^{2/3}T_d^{1/3} = 0.788(0.92 \text{ s})^{2/3}(480 \text{ s})^{1/3} \approx 5.85 \text{ s}$. The b_{opt} value derived from Eq. 13 was used in this study. Fig. 13 includes the autocorrelation function and histogram of L_u^x estimates corresponding to B = 4000 bootstrap replications. A mean L_u^x value of 4.57 m was obtained with a standard deviation of 0.51 m. Fig. 13 indicates that the original integral length scale obtained by the GCA algorithm during the iteration process of EVT07 ($L_u^x = 5.06$ m) is approximately 10.7% higher than the mean value ($L_u^x = 4.57$ m) obtained from the bootstrap statistical analysis. A least-squares (LSQ) Gaussian fit of the histogram and bootstrap statistics for other B values (to assess statistical stability) are summarized in Table 5.

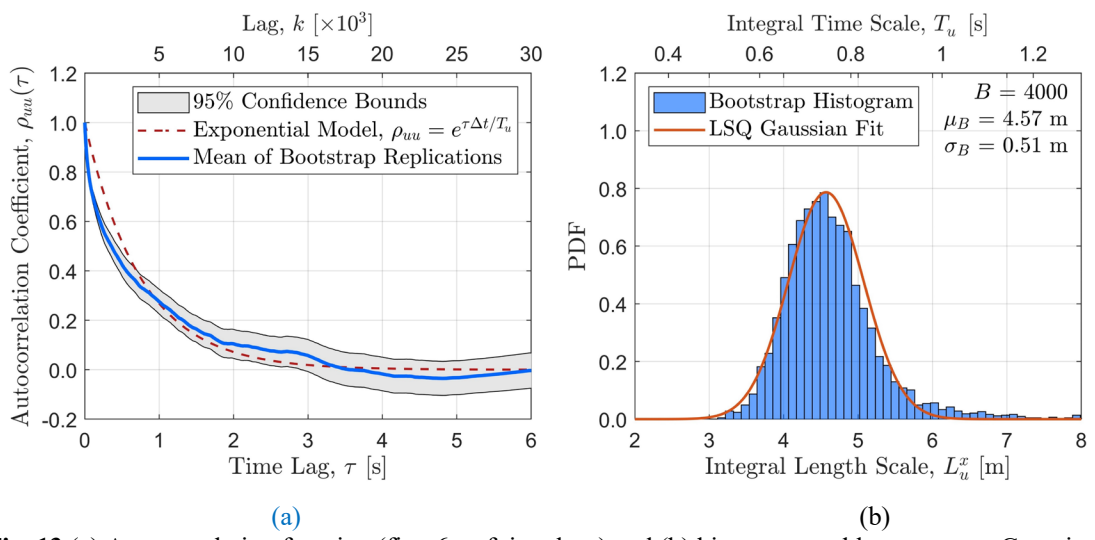


Fig. 13 (a) Autocorrelation function (first 6 s of time lags) and (b) histogram and least-squares Gaussian fit of the bootstrapped integral time (T_u) and length (L_u^x) scales for B = 4000

Table 5 Statistics of integral length scale (L_x^y) for different B bootstrap replications (EVT07; $T_d = 480$ s)

	- 6	8 (u	/		()	<u>u) </u>	
Number of Bootstrap Replications, B	Statistics of Boo $(b_{opt}\Delta t = 5.97)$	otstrap Replication s)	ns	Least-Squares (LSQ) Gaussian Fit			
	Mean, μ_B [m]	Standard Deviation, σ_B [m]	$\mu_B \pm 1.96\sigma_B$ (95% confidence interval) [m]	Mean, μ_{LSQ} [m]	Standard Deviation, σ_{LSQ} [m]	$\mu_{LSQ} \pm 1.96\sigma_B$ (95% confidence interval) [m]	
100	4.60	0.52	$4.60 \pm 22\%$	4.73	0.70	$4.73 \pm 29\%$	
500	4.53	0.48	$4.53 \pm 21\%$	4.70	0.77	$4.70 \pm 32\%$	
1000	4.61	0.50	$4.61 \pm 21\%$	4.67	0.73	$4.67 \pm 30\%$	
4000	4.57	0.51	$4.57 \pm 22\%$	4.66	0.73	$4.66 \pm 31\%$	

3.6 Conditional analysis of Reynolds stress

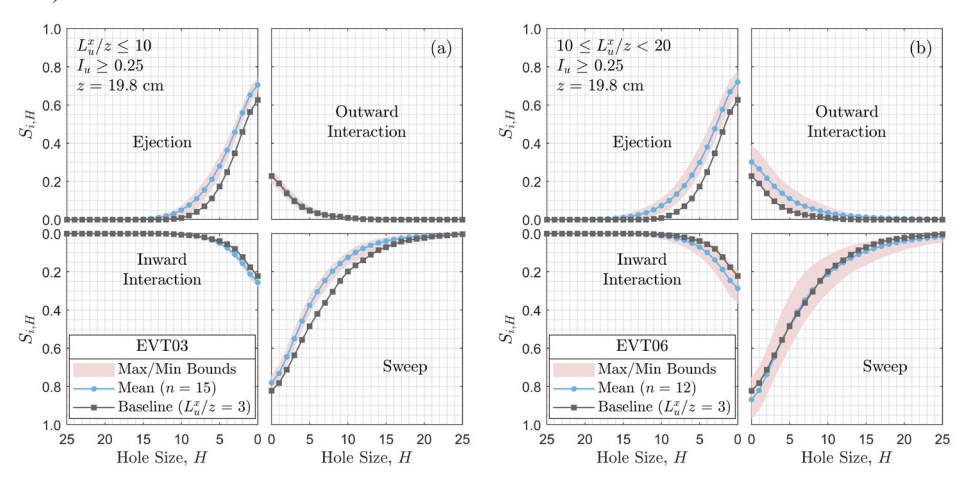
Quadrant (or conditional) analysis of mean Reynolds stress (u'w') enables greater insight into the turbulent mechanisms of organized structures measured near the canopy of rough surfaces (Lu et al. 1973; Raupach 1981; Zhu et al., 2007; Shing et al., 2023). This analysis technique applies conditional statistical averaging to partition the contribution of the mean Reynolds shear stress into four events (i.e., quadrants) based on the sign of the (mean-removed) longitudinal (u') and vertical (w') wind velocity components. The sum of the contributions of different types of events. Sweep (i = 4; u' > 0, w' < 0) and ejection (i = 2; u' < 0, w' > 0) events (quadrants two and four) make positive contributions to the Reynolds stress. Quadrants one and three correspond to inward (i = 3; u' < 0, w' < 0) and outward (i = 1; u' > 0, w' > 0) interaction events and contribute negatively to the shear stress. The contribution of the total Reynolds stress from quadrant i is

$$\langle u'w'\rangle_{i,H} = \lim_{T \to \infty} \frac{1}{T} \int_0^{T_d} u'(t)w'(t)F_{i,H}[u'(t),w'(t)] dt$$
 (16)

where T_d is the averaging time and $F_{i,H}$ is the indicator function. $F_{i,H} = 1.0$ if $|u'w'| \ge H|\overline{u'w'}|$, otherwise, $F_{i,H} = 0$. Increasing the hyperbolic "hole size" H allows investigation of large-scale and sparse structures (i.e., coherent motions) by eliminating small and frequent contributions. The fraction of the shear stress transported is obtained from

$$S_{i,H} = \frac{\langle u'w' \rangle_{i,H}}{\overline{u'w'}} \tag{17}$$

Fig. 14 illustrates the Reynolds stress fraction $|S_{i,H}|$ measured at z=19.8 cm for the four roughest GCA events $(I_{u,T}=0.3)$. For comparison, $|S_{i,H}|$ for the baseline case (i.e., no FFM) with turbulence intensity of 28% (Baseline 3 in Table 3) is included in the four subplots. The blue curves in Fig. 14 represent the mean $|S_{i,H}|$ for all GCA iterations of that EVT satisfying $I_u \geq 25\%$ and the specified L_u^x/z thresholds, while the light red patch indicated the maximum and minimum $|S_{i,H}|$ bounds of the sample. Very similar $|S_{i,H}|$ contributions are observed in EVT03 $(L_u^x/z \leq 10)$ compared to the baseline case $(L_u^x/z=3)$. The contribution of sweep events for the four L_u^x/z regimes generally match the baseline case. However, a noticeable increase in the contribution of ejections and outward interactions is evident in velocity fluctuations with $L_u^x/z > 10$ (i.e., EVT06, EVT09, and EVT12). For instance, in the case of EVT12 (Fig. 14d) and H=0, the stress fraction for outward interactions nearly doubles (from ~ 0.2 to ~ 0.39). Further, Fig. 14d also reveals large-scale sweep events in which $\sim 10\%$ exceeded nearly 20 times the mean Reynolds stress (i.e., $|S_{i=4,H=20}|=0.1$).



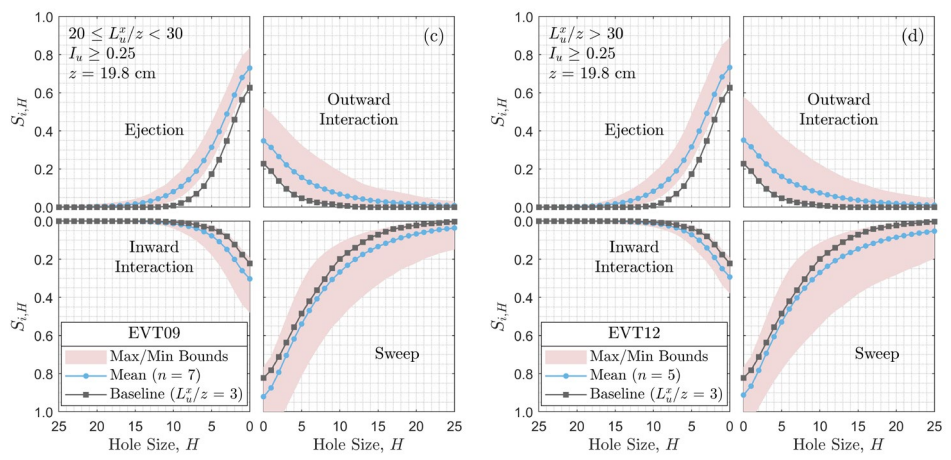


Fig. 14 Reynolds stress fraction $|S_{i,H}|$ for multiple integral length scale regimes

Past authors (Lu et al. 1973; Raupach 1981; Zhu et al., 2007; Shing et al., 2023) have often considered measuring the difference (imbalance) of stress contributions between sweep (i = 4) and ejection (i = 2) events, which can be expressed as

$$\Delta S_H = S_{4,H} - S_{2,H} \tag{18}$$

For instance, $\Delta S_H > 0$ indicate records where sweeps dominate over ejection events. Additionally, previous research involving wind tunnel experiments of instantaneous (single-point) u' and w' measurements under highly rough upstream surfaces have revealed a strong link between ΔS_H and third order statistical moments (i.e., skewness) of the velocity signal.

The imbalance of sweep and ejection events (ΔS_H ; H=0) measured at z=19.8 cm for GCA u' and w' records with $I_u \geq 25\%$ are highlighted in Fig. 15. Marker colors (and styles) represent different L_u^x/z regimes. Most of the records display sweep dominance and positive longitudinal skewness (γ_{3u}) values. When comparing the four L_u^x/z regimes, both ΔS_0 and γ_{3u} appear to increase slightly with L_u^x/z . For example, the four records with the highest γ_{3u} correspond to normalized length scales $L_u^x/z > 20$. In contrast, the smallest ΔS_0 and γ_{3u} were mainly generated by records in the lowest length scale regime ($L_u^x/z \leq 10$).

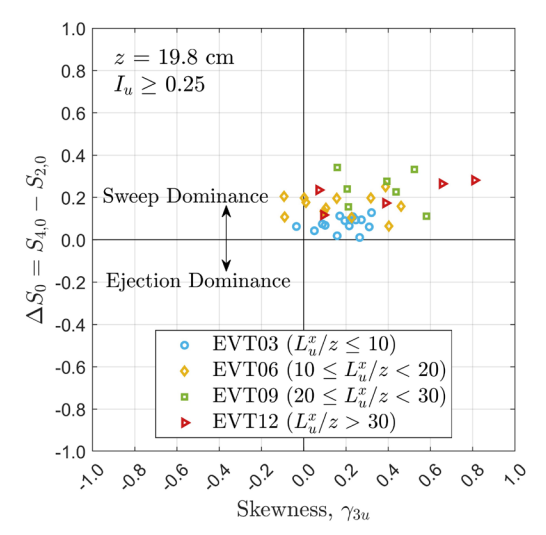


Fig. 15 Reynolds stress fraction difference (ΔS_0) and longitudinal skewness (γ_{3u}) for multiple integral length scale regimes

437 4 Discussion

4.1 Physical limits of achievable integral length scales

The results highlighted in the previous section suggest that iterative adjustments to FFM and Terraformer inputs can aid in effectively converging to desired mean and turbulent profile flows at the BLWT test section (x = 31.52 m). In the present study, the L_u^x targets (ranging between 1 m and 7 m at z = 19.8 cm) were chosen based on baseline L_u^x estimates obtained from flow measurements performed at the UF BLWT (Fernández-Cabán and Masters, 2017; Catarelli et al., 2020) prior to the commissioning of the FFM (i.e., at the time, flow conditioning consisted primarily of (constant) vaneaxial fan speeds and fully uniform Terraformer heights). As reported in Table 3, L_u^x estimates for baseline cases ranged from 0.58 m to 1.07 m and their magnitudes seemed to increase with decreasing I_u . Therefore, the lower end of realizable L_u^x at z = 19.8 cm (x = 31.52 m) appears to occur for highly rough Terraformer conditions (e.g., $I_u > 25$ %) and the exclusion of FFM-generated low-frequency velocity fluctuations. However, the intensity of the mean wind field (e.g., Reynolds number) may influence the smallest integral length scales.

Research relating to the upper limit of attainable FFM-generated integral length scales is still ongoing at the UF BLWT. However, preliminary flow measurements indicate that improved control and a broader range of L_u^x can be attained for mean wind velocities at around ~6 m/s (z=19.8 cm, which corresponds to the target \bar{u} used in this study) versus higher \bar{u} . One possible explanation is that slower \bar{u} (primarily driven by the vaneaxial fans) provides the FFM additional time to properly embed large scale turbulent fluctuations that can be conserved as the eddies advect over the Terraformer and (eventually) the testing section (i.e., measurement location). Further, noticeably larger L_u^x estimates (i.e., target overshoots) were observed during GCA iterations (see Fig. 5), which demonstrate the potential for achieving length scales greater than the range of target L_u^x adopted in this work. Yet, for point measurements close to the ground, the maximum L_u^x may be lower due to the abundance of smaller (mechanically-generated) eddies near the Terraformer canopy that can disrupt larger (FFM-generated) gust structures.

4.2 Balancing FFM and Terraformer inputs to satisfy I_u and L_u^x targets

Baseline velocity flow measurements obtained under traditional UF BLWT configurations (no active large-scale turbulence generation) relied solely on the Terraformer roughness grid to adjust the turbulence at x=31.52 m. When comparing the optimal (best GCA) Terraformer configurations for the highest I_u case (30%) across all L_u^x regimes considered, it is evident that both the FFM and roughness grid contribute to reaching the target turbulence levels at the downwind test section. The capability of the GCA scheme to reach highly turbulent levels ($I_u=0.3$) with shorter roughness element heights (especially Terraformer TF6; see Table 4) is one indication of the relevant role of L_u^x and its contributions to the turbulence intensity.

Differences in optimal Terraformer configurations for the same target I_u (i.e., decreased roughness element heights for higher target L_u^x) seemed to influence the distribution of organized (coherent) motions captured by the velocity probes located at z=19.8 cm. Examination of the instantaneous u' and w' flow components revealed a greater contribution of outward interaction events (i.e., u'>0, w'>0) to the mean Reynolds stress for larger L_u^x regimes. This trend may be directly related to the coupled effect of lower roughness elements (less near-wall turbulent mixing) and a greater contribution of large-scale turbulence to I_u . The rough-to-smooth transition immediately downwind of the Terraformer fetch (x=29.5 m) may also influence the longitudinal and vertical turbulent fluctuations detected at the measurement location.

4.3 Control of lateral and vertical integral length scales

Although, the present work was limited to active control of large-scale turbulent flow fluctuations in the longitudinal (streamwise) direction, FFM capabilities for modulating the spanwise (lateral) and vertical velocity components are presently being investigated. The autocorrelation subplots of the vertical flow velocity component presented in Fig. 11 displays gradual increase in vertical integral length scales (L_w^x) , likely a byproduct of streamwise turbulent modulations. Lateral homogeneity enforced across FFM cell rows (i.e., perfectly correlated low-frequency velocity time traces were given to cell rows) prevented the production of larger scale eddies in the spanwise direction.

It is hypothesized that greater control of large-scale turbulent structures in all three orthogonal directions is expected for x-measurement locations upstream to the test section (i.e., closer to the 2D FFM fan array). While the results demonstrate that a relatively broad range of target L_u^x can be achieved at x = 31.52 m, active and independent control of FFM-generated lateral and vertical length scales may present a greater challenge due to inherent coupling between 3D flow components. Further, 3D flow measurement experiments at x-locations closer to the FFM may

improve control of large-scale turbulence but, at the same time, limit the natural boundary layer growth via the Terraformer roughness grid.

5 Conclusions

This study investigated the effectiveness of a novel multi-fan flow control instrument for injecting large-scale (low frequency) turbulent gust structures into a large BLWT. The instrument comprises a 2D 319-fan array located in the upwind portion of the BLWT. The system operated in conjunction with an automated roughness grid to simulate small- and large-scale turbulent structures of atmospheric boundary layer flows. A series of 3D velocity profile measurements were carried out at the center of the BLWT testing section. Key observations resulting from the present work can be summarized as follows:

495 496 497

498

499

500

501

502

503

504

505

506

507

508 509

510

489

490

491

492

493

494

- 1) Depending on the target turbulence levels (i.e., I_u), the maximum observed FFM-generated longitudinal (streamwise) integral length scales (L_u^x) in the BLWT were approximately 6.4–8 m at the reference probe height of z = 19.8 cm, which were around 5.9-12.8 times greater than L_u^x estimates obtained from conventional (baseline) BLWT flow experiments (i.e., no actively generated low-frequency fluctuations).
- 2) A greater contribution of (actively-generated) large-scale (low frequency) gusts to the turbulence intensity was observed, which resulted in reduced reliance on the Terraformer roughness grid to achieve highly turbulent conditions at the test section.
- 3) A slight rise in vertical integral length scales (L_w^x) were detected with increasing L_u^x .
- 4) For velocity records with the highest target turbulence intensity (30%), conditional analysis of the Reynolds shear stress $(\overline{u'w'})$ revealed a dependence in the contribution of ejection (u' < 0, w' > 0) and outward interaction (u' > 0, w' > 0) events as the target L_u^x was systematically increased.
- 5) Sweep events (u' > 0, w' < 0) appeared to be insensitive to L_u^x for the reference measurement height and turbulent flow regimes considered. Yet, additional studies are needed to further examine the effect of L_u^x on the contributions to the Reynolds stress in highly rough conditions.
- Future work will explore the physical (mainly upper) limits of achievable FFM-generated length scales in the BLWT and their impact on near-wall turbulence. Subsequent studies will also focus on the potential for modulating lateral and vertical turbulence intensities and scales by introducing horizontal inhomogeneity into horizontally adjacent FFM cells. Finally, future research will center on systematic characterization of integral length scale effects on bluff body aerodynamics (e.g., surface pressures acting on low-rise buildings) under highly turbulent BLWT flows with precisely modulated small- and large-scale turbulence.

517 6 Acknowledgements

- The authors would like to acknowledge the DesignSafe-CI web-based research platform for the storage and curation of experimental data (Rathje et al., 2017). The authors also wish to recognize the Powell Structures and Materials Laboratory staff, with special thanks to Scott Powell, Tai-An Chen, Ian Van Voris, Justin Davis, and Rudy Wilder for their contribution in wind tunnel testing and assisting in the development of Matlab and LabVIEW code for data
- 522 acquisition and analysis.

7 Declaration

524 Competing Interests

The authors declare that they have no known competing interests that could have appeared to influence the work reported in this paper.

527 528

523

Authors' Contribution

N.M. and P.F.C. wrote the main manuscript text, N.M. prepared figures 5-10, and P.F.C. created the remaining figures (including the graphical abstract). R.C. developed the BLWT control algorithms and a portion of the data processing and analysis scripts. All authors reviewed the manuscript.

532

533 Funding

- This work is supported by the National Science Foundation (NSF) under Grant No. 2138414 and 2317176. The authors
- also acknowledge the NSF NHERI EF awardees under Grant No. 2037725. Any opinions, findings, and conclusions

or recommendations expressed in this material are those of the authors and do not necessarily reflect the views of

537 NSF.

538539

Availability of Data and Materials

- The curated dataset of flow velocity time series and relevant metadata is publicly available and can be accessed in the
- DesignSafe-CI Data Depot repository (see Mokhtar et al., 2023).
- 542 **8 References**
- ASCE 7-22 (2022). Minimum Design Loads for Buildings and Other Structures, American Society of Civil Engineers, Reston, VA.
- ASCE 49-21 (2021). Wind Tunnel Testing for Buildings and Other Structures, American Society of Civil Engineers, Reston, VA.
- 547 Azzam, A., & Lavoie, P. (2023). Unsteady flow generation in a wind tunnel using an active grid. *Experiments in Fluids*, *64*(2), 29.
- Barlow, J. B., Rae, W. H., & Pope, A. (1999). Low-speed wind tunnel testing. John wiley & sons.
- Bienkiewicz, B., Cermak, J. E., Peterka, J. A., & Scanlan, R. H. (1983). Active modeling of large-scale turbulence. *Journal of Wind Engineering and Industrial Aerodynamics*, *13*(1-3), 465-475.
- Cao, S., Nishi, A., Kikugawa, H., & Matsuda, Y. (2002). Reproduction of wind velocity history in a multiple fan wind tunnel. *Journal of wind engineering and industrial aerodynamics*, 90(12-15), 1719-1729.
- Catarelli, R. A., Fernández-Cabán, P. L., Masters, F. J., Bridge, J. A., Gurley, K. R., & Matyas, C. J. (2020a).
 Automated terrain generation for precise atmospheric boundary layer simulation in the wind tunnel. *Journal of Wind Engineering and Industrial Aerodynamics*, 207, 104276.
- Catarelli, R. A., Fernández-Cabán, P. L., Phillips, B. M., Bridge, J. A., Masters, F. J., Gurley, K. R., & Prevatt, D.
 O. (2020b). Automation and new capabilities in the university of Florida NHERI Boundary Layer Wind
 Tunnel. Frontiers in Built Environment, 6, 558151.
- Cermak, J. E., & Cochran, L. S. (1992). Physical modelling of the atmospheric surface layer. *Journal of Wind Engineering and Industrial Aerodynamics*, 42(1-3), 935-946.
- Cheung, J. C., Eaddy, M., & Melbourne, W. H. (2003). Active generation of large scale turbulence in a boundary layer wind tunnel. In *Australasian Wind Engineering Society Workshop (10th: 2003: Sydney, Australia)*.
- Cook, N. J. (1978). Wind-tunnel simulation of the adiabatic atmospheric boundary layer by roughness, barrier
 and mixing-device methods. *Journal of Wind Engineering and Industrial Aerodynamics*, 3(2-3), 157 176.
- Gan Chowdhury, A., Zisis, I., Irwin, P., Bitsuamlak, G., Pinelli, J. P., Hajra, B., & Moravej, M. (2017). Largescale experimentation using the 12-fan wall of wind to assess and mitigate hurricane wind and rain impacts on buildings and infrastructure systems. Journal of Structural Engineering, 143(7), 04017053.
- Cui, W., Zhao, L., Cao, S., & Ge, Y. (2021). Generating unconventional wind flow in an actively controlled multifan wind tunnel. *Wind Struct*, *33*, 115-122.
- Fernández-Cabán, P. L., & Masters, F. J. (2017). Near surface wind longitudinal velocity positively skews with increasing aerodynamic roughness length. Journal of Wind Engineering and Industrial Aerodynamics, 169, 94-105.
- 575 Foken, T., & Nappo, C. J. (2008). Micrometeorology. Springer Science & Business Media.
- Garcia, C. M., Jackson, P. R., & Garcia, M. H. (2006). Confidence intervals in the determination of turbulence parameters. Experiments in fluids, 40, 514-522.
- Gartshore, I. S. (1984). Some effects of upstream turbulence on the unsteady lift forces imposed on prismatic twodimensional bodies. J. Fluids Eng., 106(4), 418-424.

- Gramespacher, C., Albiez, H., Stripf, M., & Bauer, H. J. (2019). The generation of grid turbulence with continuously adjustable intensity and length scales. *Experiments in Fluids*, *60*, 1-15.
- Hideharu, M. (1991). Realization of a large-scale turbulence field in a small wind tunnel. *Fluid Dynamics Research*, 8(1-4), 53.
- Hillier, R. and Cherry, N. J. (1981). The effects of stream turbulence on separation bubbles. J. Wind Eng. Ind. Aerodyn. 8(1-2), 49-58.
- Irwin, P. A. (2008). Bluff body aerodynamics in wind engineering. *Journal of Wind Engineering and Industrial Aerodynamics*, *96*(6-7), 701-712.
- Katul, G., Poggi, D., Cava, D., & Finnigan, J. (2006). The relative importance of ejections and sweeps to momentum transfer in the atmospheric boundary layer. Boundary-layer meteorology, 120, 367-375.
- Knebel, P., Kittel, A., & Peinke, J. (2011). Atmospheric wind field conditions generated by active grids. Experiments in fluids, 51, 471-481.
- Kobayashi, H., & Hatanaka, A. (1992). Active generation of wind gust in a two-dimensional wind tunnel. *Journal of Wind Engineering and Industrial Aerodynamics*, 42(1-3), 959-970.
- Kobayashi, H., Hatanaka, A., & Ueda, T. (1994). Active simulation of time histories of strong wind gust in a wind tunnel. Journal of wind engineering and industrial aerodynamics, 53(3), 315-330.
- Larssen, J. V., & Devenport, W. J. (2011). On the generation of large-scale homogeneous turbulence. Experiments in fluids, 50, 1207-1223.
- Levitan, M. L., & Mehta, K. C. (1992a). Texas Tech field experiments for wind loads part 1: building and pressure measuring system. *Journal of Wind Engineering and Industrial Aerodynamics*, 43(1-3), 1565-1576.
- 600 Levitan, M. L., & Mehta, K. C. (1992b). Texas Tech field experiments for wind loads part II: meteorological 601 instrumentation and terrain parameters. *Journal of Wind Engineering and Industrial Aerodynamics*, 43(1-602 3), 1577-1588.
- Li, Q. S., & Melbourne, W. H. (1995). An experimental investigation of the effects of free-stream turbulence on streamwise surface pressures in separated and reattaching flows. Journal of wind engineering and industrial aerodynamics, 54, 313-323.
- 606 Lu, S. S., & Willmarth, W. W. (1973). Measurements of the structure of the Reynolds stress in a turbulent 607 boundary layer. Journal of Fluid Mechanics, 60(03), 481-511.
- Melbourne, W.H. (1979). Turbulence effects on maximum surface pressures, a mechanism and possibility of reduction, Proc. 5th Int. Conf. on Wind Engineering, Colorado, USA, Pergamon Press, pp 541-552.
- Mokhtar, N., P. Fernández-Cabán, R. Catarelli. (2023) "Generation of Large-Scale Gust Structures in a Large
 Boundary Layer Wind Tunnel: 3D Flow Measurement Experiments", in Physical Simulation of TerrainInduced and Large-Scale Turbulence Effects on the Effectiveness of Wind Mitigation Strategies for
 Low-Rise Buildings. DesignSafe-CI. https://doi.org/10.17603/ds2-0m8r-my92 v1
- Mooneghi, M. A., Irwin, P., & Chowdhury, A. G. (2016). Partial turbulence simulation method for predicting peak wind loads on small structures and building appurtenances. Journal of Wind Engineering and Industrial Aerodynamics, 157, 47-62.
- Morrison, M. J., & Kopp, G. A. (2018). Effects of turbulence intensity and scale on surface pressure fluctuations on the roof of a low-rise building in the atmospheric boundary layer. Journal of Wind Engineering and Industrial Aerodynamics, 183, 140-151.
- Neuhaus, L., Berger, F., Peinke, J., & Hölling, M. (2021). Exploring the capabilities of active grids. *Experiments in Fluids*, *62*(6), 130.
- Nishi, A., Miyagi, H., & Higuchi, K. (1993). A computer-controlled wind tunnel. Journal of Wind Engineering and Industrial Aerodynamics, 46, 837-846.
- Nishi, A., & Miyagi, H. (1995). Computer-controlled wind tunnel for wind-engineering applications. Journal of wind engineering and industrial aerodynamics, 54, 493-504.

- Nishi, A., Kikugawa, H., Matsuda, Y., & Tashiro, D. (1997). Turbulence control in multiple-fan wind tunnels. Journal of wind engineering and industrial aerodynamics, 67, 861-872.
- Nishi, A., Kikugawa, H., Matsuda, Y., & Tashiro, D. (1999). Active control of turbulence for an atmospheric boundary layer model in a wind tunnel. Journal of wind engineering and industrial aerodynamics, 83(1-3), 409-419.
- Ozono, S., Nishi, A., & Miyagi, H. (2006). Turbulence generated by a wind tunnel of multi-fan type in uniformly active and quasi-grid modes. Journal of Wind Engineering and Industrial Aerodynamics, 94(4), 225-240.
- Ozono, S., & Ikeda, H. (2018). Realization of both high-intensity and large-scale turbulence using a multi-fan wind tunnel. *Experiments in Fluids*, *59*, 1-12.
- Pinyochotiwong. (2022). Advancing the Active Flow Control of Boundary Layer Wind Tunnels. Dissertation, University of Florida.
- Politis, D. N., & White, H. (2004). Automatic block-length selection for the dependent bootstrap. Econometric reviews, 23(1), 53-70.
- Raupach, M. R. (1981). Conditional statistics of Reynolds stress in rough-wall and smooth-wall turbulent boundary layers. Journal of Fluid Mechanics, 108, 363-382.
- Rathje, E. M., Dawson, C., Padgett, J. E., Pinelli, J. P., Stanzione, D., Adair, A., ... & Mosqueda, G. (2017).

 DesignSafe: New cyberinfrastructure for natural hazards engineering. *Natural Hazards Review*, 18(3),
 06017001.
- Richards, P. J., Hoxey, R. P., Connell, B. D., & Lander, D. P. (2007). Wind-tunnel modelling of the Silsoe Cube. *Journal of Wind Engineering and Industrial Aerodynamics*, *95*(9-11), 1384-1399.
- Roadman, J., & Mohseni, K. (2009). Large scale gust generation for small scale wind tunnel testing of atmospheric turbulence. In *39th AIAA Fluid Dynamics Conference* (p. 4166).
- Saathoff, P. J., & Melbourne, W. H. (1997). Effects of free-stream turbulence on surface pressure fluctuations in a separation bubble. Journal of Fluid Mechanics, 337, 1-24.
- Shaw, R. H., & Pereira, A. R. (1982). Aerodynamic roughness of a plant canopy: a numerical experiment. *Agricultural Meteorology*, 26(1), 51-65.
- Shig, L., Babin, V., Shnapp, R., Fattal, E., Liberzon, A., & Bohbot-Raviv, Y. (2023). Quadrant Analysis of the Reynolds Shear Stress in a Two-Height Canopy. Flow, Turbulence and Combustion, 1-23.
- Shuyang, C., Nishi, A., Hirano, K., Ozono, S., Miyagi, H., Kikugawa, H., ... & Wakasugi, Y. (2001). An actively controlled wind tunnel and its application to the reproduction of the atmospheric boundary layer. *Boundary-layer meteorology*, 101, 61-76.
- 658 Simiu, E., & Yeo, D. (2019). Wind effects on structures: Modern structural design for wind. John Wiley & Sons.
- Standohar-Alfano, C. D., Estes, H., Johnston, T., Morrison, M. J., & Brown-Giammanco, T. M. (2017). Reducing
 losses from wind-related natural perils: Research at the IBHS research center. Frontiers in Built
 Environment, 3, 9.
- Stathopoulos, T., & Surry, D. (1983). Scale effects in wind tunnel testing of low buildings. Journal of Wind Engineering and Industrial Aerodynamics, 13(1-3), 313-326.
- Tieleman, H. W., Reinhold, T. A., & Marshall, R. D. (1978). On the wind-tunnel simulation of the atmospheric surface layer for the study of wind loads on low-rise buildings. *Journal of Wind Engineering and Industrial Aerodynamics*, 3(1), 21-38.
- Tieleman, H. W. (2003). Wind tunnel simulation of wind loading on low-rise structures: a review. *Journal of wind engineering and industrial aerodynamics*, 91(12-15), 1627-1649.
- Von Karman, T. (1948). Progress in the statistical theory of turbulence. *Proceedings of the National Academy of Sciences*, *34*(11), 530-539.

Zhu, W., van Hout, R., & Katz, J. (2007). On the flow structure and turbulence during sweep and ejection events
 in a wind-tunnel model canopy. Boundary-layer meteorology, 124, 205-233.